Phase Transitions

Deutsche Ausgabe: DOI: 10.1002/ange.201505487
Internationale Ausgabe: DOI: 10.1002/anie.201505487

Direct Observation of an Anomalous Spinel-to-Layered Phase Transition Mediated by Crystal Water Intercalation

Sangryun Kim, Kwan Woo Nam, Soyeon Lee, Woosuk Cho, Joo-Seong Kim, Byung Gon Kim, Yoshifumi Oshima, Ju-Sik Kim, Seok-Gwang Doo, Hyuk Chang, Doron Aurbach, and Jang Wook Choi**

Abstract: *The phase transition of layered manganese oxides to spinel phases is a well-known phenomenon in rechargeable batteries and is the main origin of the capacity fading in these materials. This spontaneous phase transition is associated with the intrinsic properties of manganese, such as its size, preferred crystal positions, and reaction characteristics, and it is therefore very difficult to avoid. The introduction of crystal water by an electrochemical process enables the inverse phase transition from spinel to a layered Birnessite structure. Scanning transmission electron microscopy can be used to directly visualize the rearrangement of lattice atoms, the simultaneous insertion of crystal water, the formation of a transient structure at the phase boundary, and layer-by-layer progression of the phase transition from the edge. This research indicates that crystal water intercalation can reverse phase transformation with thermodynamically favored directionality.*

Layered transition-metal (TM) oxides are widely used for electrodes in lithium,[1] sodium,[2] and magnesium[3] rechargeable batteries owing to their superior specific capacities. When the TM is manganese, in particular, the materials can have the additional advantages of low cost, abundance of raw materials, environmentally benign character, and relatively high operating voltages.[1,4,5] However, most Mn-containing battery electrodes have shortcomings, such as fatal dissolution[6] of Mn^{2+} and strain development from Jahn–Teller distortion[7] of Mn^{3+}. Layered manganese oxides suffer from another critical structural instability, namely a spontaneous layered-to-spinel phase transition.[8–12] In fact, all of these structural drawbacks are interrelated so that each of them can accelerate the others.

The layered-to-spinel phase transition originates from the preferred migration of Mn and is thus related to its intrinsic characteristics: 1) the high mobility of Mn ions, leading to isotropic Mn distribution;[8] 2) the favorable mixing between cations and Mn ions owing to their similar ionic radii,[9] particularly Li^+ and Mn^{3+}; and 3) the preferential migration of Mn^{2+} (generated from a disproportionation reaction of Mn^{3+}) to tetrahedral sites.[10] Various efforts to suppress the migration of Mn, including the substitution of Mn by fixed-valence cations,[13,14] more electronegative transition metal ions,[14,15] and low-mobility transition-metal ions,[14,15] can be understood in the same way.

It was recently reported that spinel Mn_3O_4 can be transformed to layered Birnessite $A_xMnO_2{\cdot}yH_2O$ (A = monovalent or divalent cation) when electrochemically cycled in aqueous electrolyte solutions.[16–18] This observation is quite surprising because the phase transition is in the opposite direction to the known spontaneous process. This opposite phase transition can also provide an insight into enhancing cycle life of layered cathode materials in various rechargeable batteries. Nonetheless, we are lacking mechanistic information about these intriguing, interesting processes, and an atomic-level understanding on how this peculiar process takes place is currently unavailable. Using scanning transmission electron microscopy (STEM), in the present investigation, we reveal that the phase transition is mediated by formation of a transition phase at the phase boundary that traps crystal water in a stepwise manner. The phase transition progresses with layer-by-layer propagation of the transient phase toward the original spinel.

From the crystal structure viewpoint, the spinel (Figure 1a) and layered (Figure 1b) crystal structures have the structural basis of an ABC-packed array of oxygen atoms in common. Thus, a phase transition between these phases can be achieved without perturbing the oxygen framework. The detailed structural description is provided in the Supporting Information, Section 1. For the known phase transition from

[*] Dr. S. Kim,[+] K. W. Nam,[+] J.-S. Kim, B. G. Kim, Prof. J. W. Choi
Graduated School of EEWS and KAIST Institute NanoCentury
Korea Advanced Institute of Science and Technology (KAIST)
Daejeon, 305-701 (Korea)
E-mail: jangwookchoi@kaist.ac.kr
Dr. S. Lee[+]
Department of Electronic Chemistry, Tokyo Institute of Technology
4259 G1-1 Nagatsuta, Midori-ku, Yokohama 226-8502 (Japan)
Dr. W. Cho
Advanced Batteries Research Center
Korea Electronics Technology Institute (KETI)
25 Saenari-ro, Bundang-gu, Seongnam 463-816 (Republic of Korea)
Prof. Y. Oshima
School of Materials Science I
Japan Advanced Institute of Science and Technology
1-1 m1-61 Asahidai, Nomi, Ishikawa 923-1292 (Japan)
Dr. J.-S. Kim, Dr. S.-G. Doo, Dr. H. Chang
Material Research Center, Samsung Advanced Institute of Technology, Samsung Electronics Co., LTD
130 Samsung-ro, Yeongtong-gu, Suwon-si, Gyeonggi-do 443-803 (Republic of Korea)
Prof. D. Aurbach
Department of Chemistry and Bar-Ilan Institute of Nanotechnology and Advanced Materials, Bar-Ilan University
Ramat-Gan 5290002 (Israel)
E-mail: Doron.Aurbach@biu.ac.il
[+] These authors contributed equally to this work.

Supporting information for this article is available on the WWW under http://dx.doi.org/10.1002/anie.201505487.

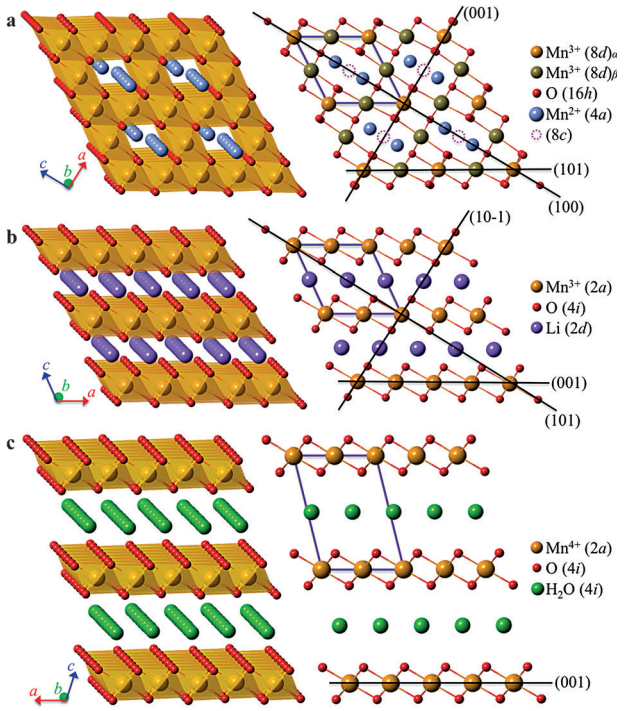

Figure 1. a) The crystal structure of Mn_3O_4. The spinel Mn_3O_4 belongs to tetragonal space group $I4_1/amd$, in which Mn^{2+} and Mn^{3+} occupy tetrahedral (4*a*) and octahedral (8*d*) sites respectively in the intervening distorted cubic close-packed array of oxygen atoms (16*h*). b) The crystal structure of $LiMnO_2$, which has a layered structure (α-$NaFeO_2$ type) with alternating layers of Li (2*d*) and Mn (2*a*) both occupying the octahedral sites of a cubic close-packed array consisting of oxygen atoms (4*i*). c) The crystal structure of Birnessite. The structure described herein is a monoclinic unit cell of cation-free Birnessite $MnO_2{\cdot}yH_2O$. The crystal water is located at the interlayer space (4*i*) between the layers of edge-sharing MnO_6 octahedra.

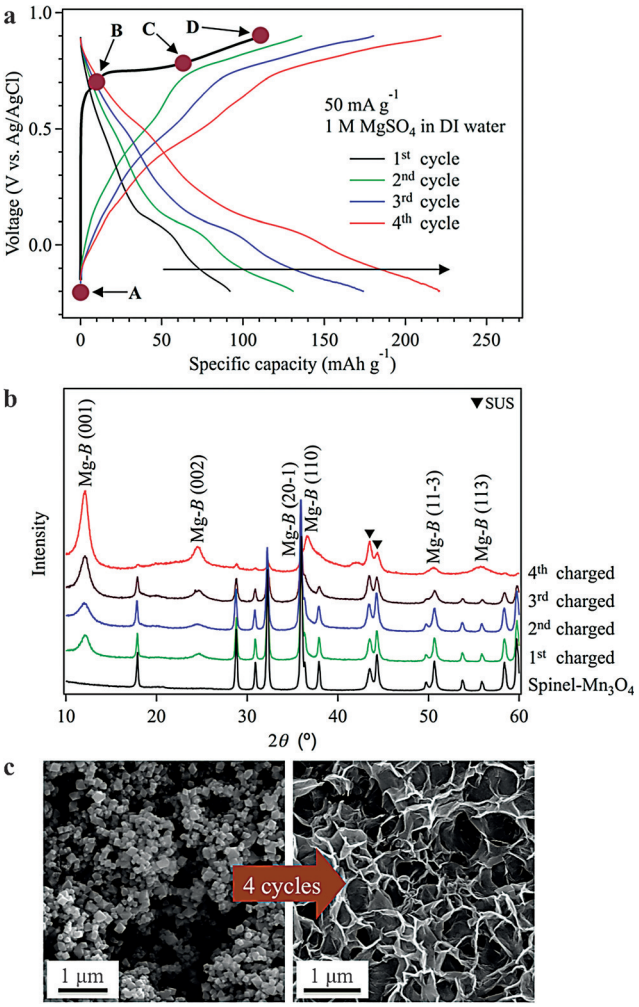

Figure 2. a) The charge–discharge profiles in 1 M $MgSO_4$ aqueous electrolyte at a rate of 50 mA g^{-1}. b) XRD patterns at different cycling stages. c) SEM images showing the morphology change from spinel Mn_3O_4 to Mg-*B*.

layered $Li_{1-x}MnO_2$ (charged state) to cubic spinel, one fourth of the $Mn^{3+/4+}$ ions in the TM layers migrate to the empty octahedral sites in the adjacent Li layers, while the Li ions move from the octahedral sites to the neighboring tetrahedral sites in the Li layers. In the monoclinic unit cell of the cation-free Birnessite $MnO_2{\cdot}yH_2O$ (Figure 1c), the crystal water is located at the interlayer space between the edge-sharing MnO_6 octahedral layers.[19]

The inverse phase transition from spinel Mn_3O_4 (dimension ca. 100 nm)[20] to the crystal water containing layered manganese Birnessite (MnO_2, denoted as Mg-*B*) was processed by an electrochemical transformation in an aqueous electrolyte solution (1M magnesium sulfate) under the galvanostatic mode (see the Supporting Information for details). During this cycling, the specific capacity increases continuously, reaching 220.1 mAh g^{-1} after 4 cycles (Figure 2a). The formation of the layered Birnessite structure after the cycling was verified by X-ray diffraction (XRD, Figure 2b), scanning electron microscopy (SEM, Figure 2c), and scanning transmission electron microscopy (STEM, Supporting Information, Figure S1; see the Supporting Information, Section 2 for a detailed description). The electrochemical cycling using various electrolyte solution conditions indicates that the phase transition is feasible only in the aqueous electrolyte solutions, reconfirming the critical role of aqueous media (thus crystal water intercalation) in the observed phase transition (Supporting Information, Figure S2).

The voltage profile in the first charge is different in appearance from those in the subsequent discharge–charge cycles (Figure 2a), which is the first indication that the phase transition is most significant in the first charge. A series of analyses during the first cycle (Supporting Information, Figure S3a) consistently verify the formation of a cation-free Mg-*B* phase during the charge process. The potential profiles in the subsequent discharge–charge cycles reflect more pronounced (de)intercalation process of Mg ions with the generated Mg-*B* (see details to support this scenario in the Supporting Information, Section 3, including XRD patterns in Figure S3b, thermogravimetric analysis (TGA) data in Figure S3c and Table S1, X-ray photoelectron spectroscopy (XPS) spectra in Figure S4, and SEM images in Figure S5). A control process starting with the discharging process indeed

produces almost zero capacity (Supporting Information, Figure S6). Based on these results, our atomic-level characterization by spherical aberration-corrected STEM focuses on the first charge.

For the four points during the first charge (denoted by point A, B, C, and D in Figure 2a), high-angle annular dark-field (HAADF) and annular bright-field (ABF) images were obtained simultaneously along the [010] zone axis of the tetragonal spinel. The STEM imaging was conducted on the thin edge region (< 5 nm) of the particle. The HAADF image of spinel Mn_3O_4 (point A in Figure 2a) shows only manganese atomic columns as bright dots owing to its *Z*-contrast:[21] the tetrahedral Mn^{2+} (4*a*) and octahedral Mn^{3+} (8*d*) sites (Figure 3a). In the (101) planes where Mn^{3+} is alternately positioned in the $(8d)_\alpha$ and $(8d)_\beta$ columns (Figure 1a), the $(8d)_\alpha$ columns (arrow 1 in Figure 3a inset) exhibited higher brightness than the $(8d)_\beta$ columns (arrow 2 in Figure 3a inset) because the available sites in the $(8d)_\alpha$ columns are occupied twice as much as those in the $(8d)_\beta$ columns (Supporting Information, Section 1). The ABF image displayed all kinds of atomic columns as dark dots: the O (16*h*) and Mn sites (Figure 3b). This observation under both modes matches well with the structure of spinel Mn_3O_4, as indicated by the overlaid atomic configuration in Figure 3b, bottom inset.

According to the STEM images at point B (0.72 V vs. Ag/AgCl), a clear phase transition is observed, as the layered (001) planes begin to appear from the bottom two outermost layers (Figure 3c,d, and their magnified images in Figure 3i,j), while all the higher layers preserve the spinel structure. For clarity, the structures discussed from here onwards will be based on the spinel coordination. In the lowermost layer (orange line), both HAADF and ABF images show almost the same contrast for the $(8d)_\alpha$ and $(8d)_\beta$ Mn columns (arrows 3 and 4 in Figure 3i and 3j), in contrast to the initial spinel structure (see the spinel structure in the upper layers with distinct contrast between the columns by following the green dotted line). On the other hand, in the (202) layer (orange dotted line) immediately above the lowest layer, the intensity of the octahedral (8*c*) columns (arrow 5 in Figure 3i) is far higher than that of the tetrahedral (4*a*) columns (arrow 6 in Figure 3i). This distinct contrast between the columns is indeed opposite to the equivalent columns in the spinel (see arrows 5′ and 6′ pointing to the respective octahedral (8*c*) and tetrahedral (4*a*) columns in the spinel phase with reversed contrast). This phenomenon is attributed

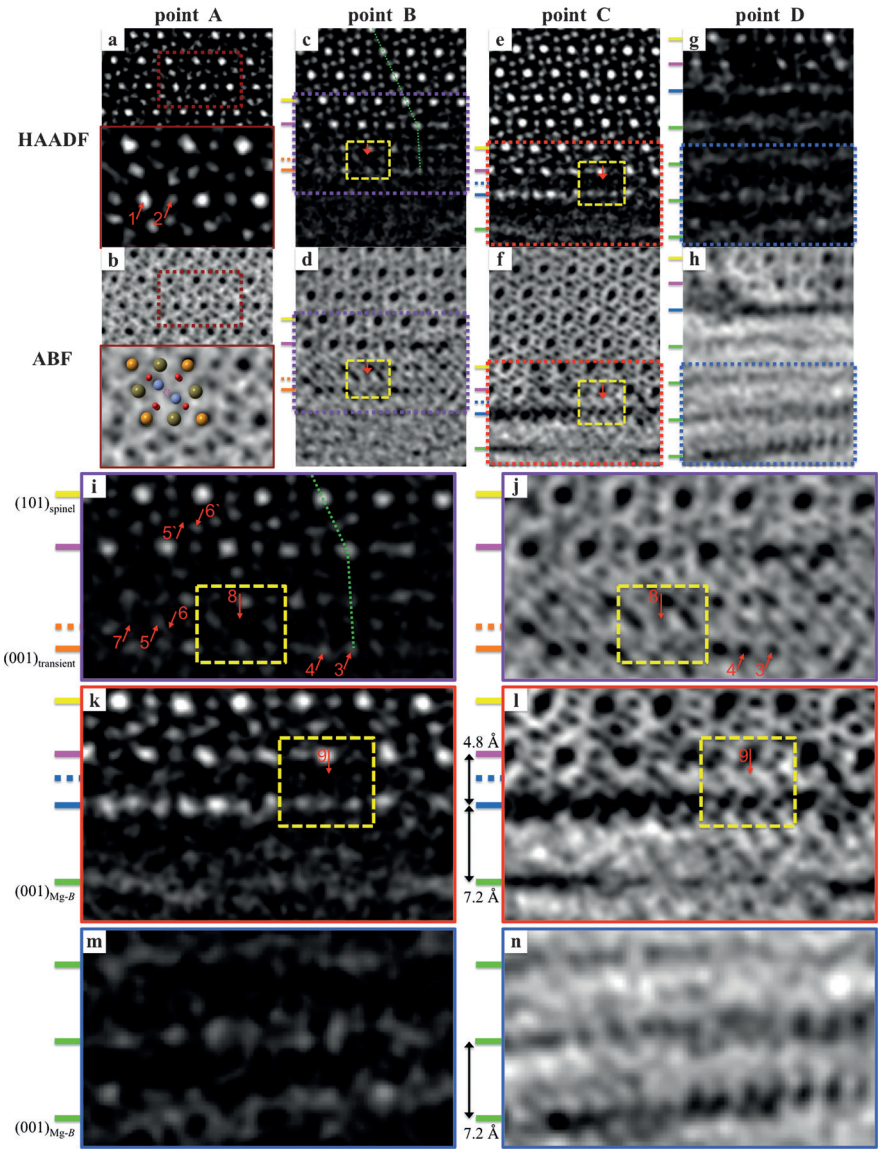

Figure 3. The HAADF and ABF images of the thin-edge region of the particles at −0.2 (point A, Mn_3O_4), 0.72 (point B), 0.77 (point C), and 0.90 (point D, fully charged) V vs. Ag/AgCl marked during the first charge in Figure 2a. a) HAADF and b) ABF images at point A. Insets: Magnified images from the red dotted boxes. Mn^{3+} $(8d)_\alpha$ orange, Mn^{3+} $(8d)_\beta$ khaki, Mn^{2+} (4*a*) blue, O (16*h*) red, O (8*c*) pink dotted circle. The same analyses at points c),d) B, e),f) C, and g),h) D. The magnified i) HAADF and j) ABF images are from the purple marked areas in (c) and (d), respectively. $(101)_{spinel}$ plane yellow, $(101)_{spinel}/(001)_{transient}$ boundary pink, $(202)_{spinel}/(002)_{transient}$ boundary orange-dotted, $(001)_{transient}$ plane orange lines. The magnified k) HAADF and l) ABF images are from the red marked area in (e) and (f), respectively. The magnified m) HAADF and n) ABF images are from the blue marked area in (g) and (h), respectively. $(101)_{spinel}$ plane yellow, $(101)_{spinel}/(001)_{transient}$ boundary pink, $(202)_{spinel}/(002)_{transient}$ boundary blue-dotted, $(001)_{transient}/(001)_{Mg\text{-}B}$ boundary blue, $(001)_{Mg\text{-}B}$ plane green lines. All the HAADF and ABF images were obtained simultaneously along the [010] zone axis of the tetragonal spinel. All the yellow dotted boxes indicate the same areas between HAADF and ABF images.

to the migration of Mn^{2+} from the tetrahedral sites to the octahedral sites. This migration can also be understood as an intermediate state in the Mn^{2+} dissolution, as the ionic conduction in the spinel framework is known to follow the 8*c*–4*a*–8*c* three-dimensional trajectory.[7] Moreover, the $(8d)_\beta$ columns (arrow 7 in Figure 3i) in the (202) layer shows very low or negligible intensity (clearly lower than that of the 4*a* and 8*c* columns). The equal intensity of the $(8d)_\alpha$ and $(8d)_\beta$ columns in the (101) layer, together with the diminished intensity of the $(8d)_\beta$ columns in the (202) layer, implies $Mn^{3+/4+}$ migration through the (202)-to-(101) pathway.

These structural changes are the reverse process of the known layered-to-spinel transition,[9–12] and are mediated by crystal water insertion. The HAADF and ABF images directly demonstrate the insertion of crystal water. Although the HAADF image (Figure 3i) displays no contrast at octahedral $(8d)_\beta$ column (arrow 8 in Figure 3i), the ABF image for the same column (Figure 3j) clearly shows dark contrast. As light elements, such as H,[22] Li,[23] and O[24] are visualized only in the ABF imaging, the dark contrast at $(8d)_\beta$ indicates the presence of oxygen or crystal water. It is unlikely that the dark contrast corresponds to an oxygen layer, because the measured distance between the (202) and (101) layer (ca. 2.4 Å) is clearly different from the distance between oxygen layers and TM layers in the conventional layered structure (ca. 1.2 Å)[4] and the Birnessite structure (ca. 1.1 Å).[19] Taking into account the electrochemical process in the aqueous phase by which the crystal water containing layered phase was formed, we conclude that the observed contrast is a signature of crystal water.

A series of the STEM images obtained at points B and C (0.77 V vs. Ag/AgCl) indicates that the phase transition towards the layered Birnessite progresses in a layer-by-layer scale from the edge by engaging a transient structure. The lowermost layer has expanded from 4.8 Å to 7.2 Å (Figure 3e and 3f, and their magnified images in Figure 3k and 3l). The second layer from the bottom has been transformed to a transient structure that is very similar to the lowermost layer at point B, as similar atomic rearrangements and contrast reflective of crystal water (arrows 9 in Figure 3k and 3l) were observed. Thus, this transient phase constitutes a phase boundary between the spinel and Birnessite phases and moves as the phase transition progresses. For the accommodation of crystal water in the transient phase with the given interlayer distance (4.8 Å), it is plausible that the water turns to hydronium ion (H_3O^+) that allows for smaller distance to the lattice oxygen atoms using its smaller ionic radius and stronger electrostatic interaction with the lattice oxygen atoms. A previous study indicates that H_3O^+ can be indeed trapped between H_2O layers, where the distance between H_3O^+ and the nearest oxygen layer is very similar[25] to that in our transient phase. A theoretical study also estimates a very similar distance between H_3O^+ and the adjacent oxygen layer.[26] Upon further insertion of crystal water, the insufficient interlayer distance increases abruptly to 7.2 Å (more detailed interpretation of the point B and C is provided in Supporting Information, Section 4, including the intensity spectrum of the STEM image in Figure S7).

The STEM images at point D (0.90 V vs. Ag/AgCl) reveal that the phase transition to Birnessite progresses further to about 4 layers (green lines in Figure 3g and 3h), reconfirming the layer-by-layer progression of the phase transition. The outer layers of the higher magnification images (Figure 3m and 3n) at this point show denser atomic contrast with more regularly aligned manganese layers. Also, the interlayer distance is observed to increase to about 7.2 Å consistently for all of the circa 4 layers, suggesting that the crystal water insertion increases the interlayer distance abruptly from 4.8 Å to 7.2 Å, rather than through any intermediate values in a progressive manner, because the crystal water insertion favors such expanded layer formation to minimize the electrostatic repulsion between the oxygen atoms of the crystal water and the framework. The abrupt phase transition is also in good agreement with the XRD patterns (Supporting Information, Figure S3b) that do not exhibit any peaks corresponding to intermediate interlayer distances (the mechanisms that take place throughout the phase transition are graphically summarized in Supporting Information, Figure S8).

The morphology change from the octahedron to the lamella structure observed in SEM characterization (Figure 2c) can also be explained in detail by analyses using lower magnification STEM (Figure 4). Both ABF images (Figure 4a,b) taken at point D display a peeling-off of lamella structure from the octahedron surface. A fast Fourier transform (FFT) pattern (Figure 4c) obtained from the image marked by the red dotted box in Figure 4b verifies that the host structure is under the spinel framework. More importantly, the FFT pattern confirmed that the peeling-off of the lamella structure is along the spinel [101] direction, which is consistent with the Birnessite formation along the same direction in the STEM images in Figure 3. From these series of high- and low-magnification STEM results, it can be speculated that once the spinel-to-Birnessite phase transition progresses over about 10 nm, the already grown Birnessite layers tend to peel off, perhaps due to unfavorable heteroboundaries between both phases. In other words, the presence of the phase boundary gives rise to strains, defects, and so on, increasing the interfacial free energy (γ).[27] γ tends to rise as the spinel-to-Birnessite phase transition progresses. Once γ reaches a critical point, the peeling-off of the grown Birnessite layers is energetically more preferred. During this process, the crystal water plays a critical role in maintaining the layered part in one entity without structural collapse via its hydrogen bonding[28] with the adjacent layer atoms. Instead, the increased γ can be concentrated at the phase boundary, leading to the peeling-off of the grown layers from this boundary. This role of crystal water was analogously identified during the synthesis of reduced graphene oxide with a strong tendency to restack.[29] In the same way, the inefficient phase transition of large spinel particles (Supporting Information, Figure S9) can be explained by their small portions of surface that are not supportive of the surface peeling-off mechanism (Supporting Information, Section 5). The peeling-off process is graphically summarized in Figure 4d.

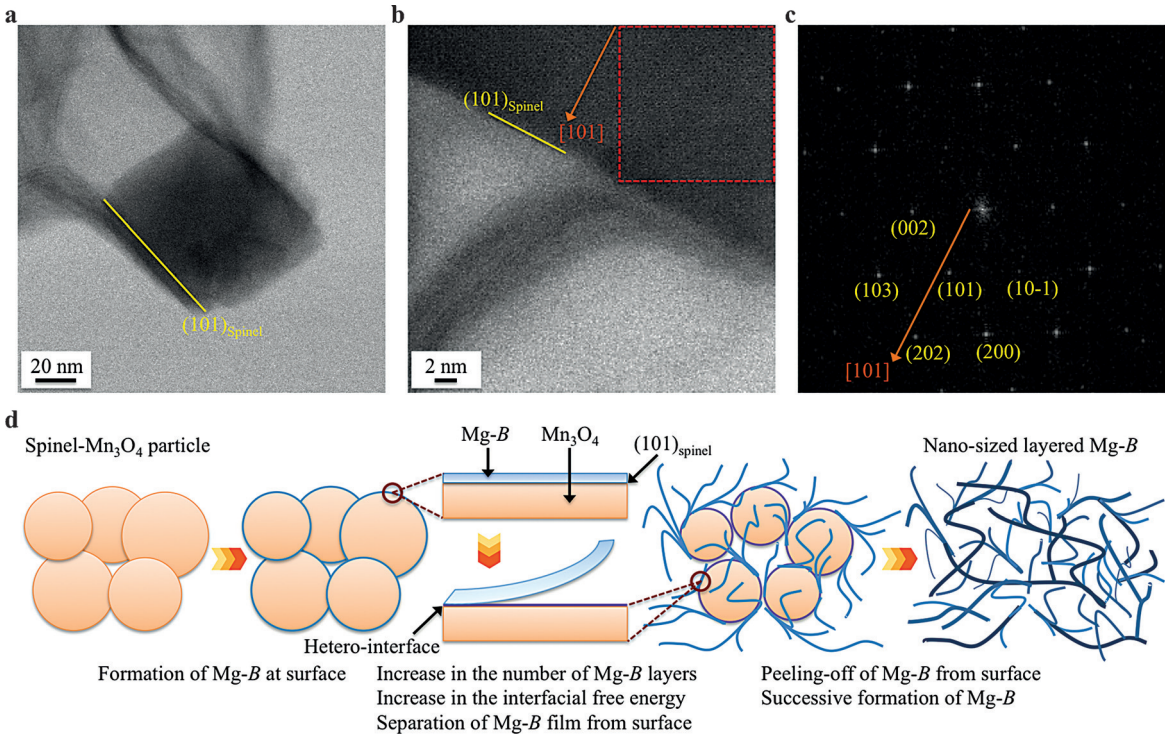

Figure 4. ABF images after the first charge at a) low and b) high magnifications. c) A fast Fourier transform (FFT) pattern from the red rectangle in (b). d) A representation of the formation process of Mg-*B* nanofilms.

In conclusion, we have closely observed the anomalous spinel-to-layered phase transition mediated by crystal water insertion. This phenomenon can be generalized by stating that crystal water insertion via aqueous activation processes can drive thermodynamically unfavorable phase transitions. From the synthesis perspective, it may be feasible to develop various synthetic routes that involve crystal water insertion for production of new nanomaterials with unconventional crystal structures.

Acknowledgements

D.A. acknowledges help from the ISF, Israel Science Foundation, in the framework of the INREP project, and thanks Dr. Judith Grinblat and Dr. Michael Talianker for helpful discussions. J.W.C. acknowledges the support by the National Research Foundation of Korea (NRF) grant funded by the Korea government (MEST) (NRF-2012-R1A2A1A01011970, (NRF-2010-C1AAA001-0029031, and NRF-2014R1A4A1003712). S.L. acknowledges the support from JST-CREST and Grant-in-Aid for Young Scientists (B) (No. 15K17434). The use of R005 microscope was supported by Tokyo Institute of Technology. This work was also supported by BK21PLUS program. This work was also made possible by NPRP grants no. 5-569-2-232 from the Qatar National Research Fund (a member of the Qatar Foundation).

Keywords: Birnessite · crystal water · layered cathode materials · phase transitions · spinels

How to cite: *Angew. Chem. Int. Ed.* **2015**, *54*, 15094–15099
Angew. Chem. **2015**, *127*, 15309–15314

[1] J. M. Tarascon, M. Armand, *Nature* **2001**, *414*, 359–367.
[2] N. Yabuuchi, K. Kubota, M. Dahbi, S. Komaba, *Chem. Rev.* **2014**, *114*, 11636–11682.
[3] H. D. Yoo, I. Shterenberg, Y. Gofer, G. Gershinsky, N. Pour, D. Aurbach, *Energy Environ. Sci.* **2013**, *6*, 2265–2279.
[4] A. R. Armstrong, P. G. Bruce, *Nature* **1996**, *381*, 499–500.
[5] M. S. Whittingham, *Chem. Rev.* **2004**, *104*, 4271–4301.
[6] R. J. Gummow, A. Dekock, M. M. Thackeray, *Solid State Ionics* **1994**, *69*, 59–67.
[7] M. M. Thackeray, W. I. F. David, P. G. Bruce, J. B. Goodenough, *Mater. Res. Bull.* **1983**, *18*, 461–472.
[8] G. Vitins, K. West, *J. Electrochem. Soc.* **1997**, *144*, 2587–2592.
[9] S. H. Kim, W. M. Im, J. K. Hong, S. M. Oh, *J. Electrochem. Soc.* **2000**, *147*, 413–419.
[10] J. Reed, G. Ceder, A. Van der Ven, *Electrochem. Solid-State Lett.* **2001**, *4*, A78–A81.
[11] S. Choi, A. Manthiram, *J. Electrochem. Soc.* **2002**, *149*, A1157–A1163.
[12] A. R. Armstrong, N. Dupre, A. J. Paterson, C. P. Grey, P. G. Bruce, *Chem. Mater.* **2004**, *16*, 3106–3118.
[13] B. Ammundsen, J. Desilvestro, T. Groutso, D. Hassell, J. B. Metson, E. Regan, R. Steiner, P. J. Pickering, *J. Electrochem. Soc.* **2000**, *147*, 4078–4082.
[14] S. Patoux, M. Dolle, M. M. Doeff, *Chem. Mater.* **2005**, *17*, 1044–1054.
[15] F. Zhang, M. S. Whittingham, *Electrochem. Solid-State Lett.* **2000**, *3*, 309–311.
[16] Y. Dai, K. Wang, J. Y. Xie, *Appl. Phys. Lett.* **2007**, *90*, 104102.
[17] S. Komaba, T. Tsuchikawa, A. Ogata, N. Yabuuchi, D. Nakagawa, M. Tomita, *Electrochim. Acta* **2012**, *59*, 455–463.

[18] K. W. Nam, S. Kim, S. Lee, M. Salama, I. Shterenberg, Y. Gofer, J.-S. Kim, E. Yang, C. S. Park, J.-S. Kim, S.-S. Lee, W.-S. Chang, S. G. Doo, Y. N. Jo, Y. Jung, D. Aurbach, J. W. Choi, *Nano Lett.* **2015**, *15*, 4071 – 4079.
[19] J. E. Post, D. R. Veblen, *Am. Mineral.* **1990**, *75*, 477 – 489.
[20] J. S. Kim, K. Kim, W. Cho, W. H. Shin, R. Kanno, J. W. Choi, *Nano Lett.* **2012**, *12*, 6358 – 6365.
[21] S. J. Pennycook, D. E. Jesson, *Ultramicroscopy* **1991**, *37*, 14 – 38.
[22] R. Ishikawa, E. Okunishi, H. Sawada, Y. Kondo, F. Hosokawa, E. Abe, *Nat. Mater.* **2011**, *10*, 278 – 281.
[23] Y. Oshima, H. Sawada, F. Hosokawa, E. Okunishi, T. Kaneyama, Y. Kondo, S. Niitaka, H. Takagi, Y. Tanishiro, K. Takayanagi, *J. Electron Microsc.* **2010**, *59*, 457 – 461.
[24] E. Okunishi, I. Ishikawa, H. Sawada, F. Hosokawa, M. Hori, Y. Kondo, *Microsc. Microanal.* **2009**, *15*, 164 – 165.
[25] K. Takada, K. Fukuda, M. Osada, I. Nakai, F. Izumi, R. A. Dilanian, K. Kato, M. Takata, H. Sakurai, E. Takayama-Muromachi, T. Sasaki, *J. Mater. Chem.* **2004**, *14*, 1448 – 1453.
[26] H. Sakuma, K. Kawamura, *Geochim. Cosmochim. Acta* **2011**, *75*, 63 – 81.
[27] J. W. Cahn, J. E. Hilliard, *J. Chem. Phys.* **1958**, *28*, 258 – 267.
[28] B. Lanson, V. A. Drits, Q. Feng, A. Manceau, *Am. Mineral.* **2002**, *87*, 1662 – 1671.
[29] D. R. Dreyer, S. Park, C. W. Bielawski, R. S. Ruoff, *Chem. Soc. Rev.* **2010**, *39*, 228 – 240.

Received: June 15, 2015
Revised: September 24, 2015
Published online: October 16, 2015

